RSC Advances

ROYAL SOCIETY OF CHEMISTRY

PAPER

View Article Online
View Journal | View Issue

Check for updates

Cite this: *RSC Adv.*, 2025, **15**, 28689

Lumbrokinase-loaded GelMA hydrogels with inflammatory regulatory capacity promote vascularized bone regeneration in critical-sized cranial defects

Yao-Wen Zhang, Sheng-Tao Zhao, Yi-Fei Ma, Yi-Hui Pan and Xiang-Zhen Yan *

Received 12th June 2025
Accepted 5th August 2025

DOI: 10.1039/d5ra04178c

rsc.li/rsc-advances

The management of critical-sized bone defects resulting from trauma and resective surgeries still poses significant clinical challenges. Factors contributing to inadequate bone regeneration in critical-sized defects are complex and multifaceted, including vascular injury and inflammation. Inspired by earthworms' remarkable regenerative abilities, we incorporated lumbrokinase (LK), an extract from earthworms, into injectable gelatin methacryloyl (GelMA) hydrogels to achieve controlled release of LK, thereby enhancing vascularized bone regeneration in critical-sized defects. While LK has been clinically utilized as an antithrombotic agent for decades in treating cerebrovascular and cardiovascular diseases, this study reveals its novel anti-inflammatory properties and dual capacity to promote both osteogenesis and angiogenesis. The LK-loaded GelMA hydrogel demonstrated favorable biocompatibility, good injectability and viscoelastic properties, tunable degradation kinetics, and optimal swelling characteristics. Comprehensive *in vitro* and *in vivo* evaluations confirmed the hydrogel's efficient LK loading and sustained release profile. The combined effects of enhanced osteogenesis, angiogenesis, and immunomodulation significantly improved critical-sized bone defect regeneration, demonstrating substantial potential of the LK-loaded GelMA hydrogel for clinical translation in the reconstruction of critical-sized bone defects.

1. Introduction

Bone can regenerate and self-repair,[1] primarily through the coordinated action of osteoblasts, osteocytes, and osteoclasts.[2] However, when defects exceed the critical size of bone's self-healing ability, they often require an extended duration for the self-healing process or are challenging to repair and augment through the natural bone growth process.[3] Such defects are defined as critical-sized defects.[4] Bone injuries related to oncological resection, trauma, and osteoporosis might result in critical-sized bone defects, posing major financial burdens for patients.[3,5]

Current regenerative strategies for critical-sized defects often utilize scaffolds constructed from synthetic or biomimetic materials, commonly integrated with bioactive compounds or therapeutic cells.[6] Nevertheless, many of them fail in facilitating optimal bone healing due to insufficient vascularization.[7] Vascularization is crucial for oxygen, nutrients, growth factors, and minerals to transfer during bone regeneration, and insufficient vascular support can delay or hinder bone formation.[8–10] Consequently, angiogenesis is of great significance to the healing of critical-sized bone defects.

Another cause of inadequate bone regeneration in critical-sized defects is immunological dysregulation,[11] with elevated reactive oxygen species (ROS) and inflammation being key contributors to this phenomenon.[12] Macrophages secrete inflammatory cytokines that impede osteoblast differentiation through increased ROS levels, thereby hindering the repair of critical-sized bone defects.[13] Furthermore, ROS-induced oxidative stress can further enhance the synthesis of pro-inflammatory cytokines, perpetuating the cycle of inflammation.[14] Therefore, disrupting the cycle of ROS and inflammation offers a promising strategy for enhancing bone regeneration.[15]

Earthworms are fascinating animals with the capacity to regenerate lost body segments.[16] Traditional Chinese medicine has used earthworms for thousands of years because of their rich nutritional content.[17] Mihara *et al.* discovered lumbrokinase (LK), an extract from the earthworm *Lumbricus rubellus*, two decades ago.[18] LK comprises a group of bioactive proteolytic enzymes with molecular weights ranging from 25 kDa to 32 kDa.[19] Clinically, LK has been applied to the treatment

---

Shanghai Engineering Research Center of Tooth Restoration and Regeneration & Tongji Research Institute of Stomatology & Department of Periodontology, Shanghai Tongji Stomatological Hospital and Dental School, Tongji University, Shanghai, 200072, P. R. China. E-mail: xiangzhenyan03@163.com; Fax: +86-21-66524025; Tel: +86-21-66313739

of strokes and cardiovascular diseases.[20,21] Recent studies found that LK exhibited cardioprotective,[22] antibacterial,[23] anti-inflammatory,[24] and osteogenesis-promoting effects.[24] Regarding its antibacterial property, LK significantly inhibited the growth of *Staphylococcus aureus* and reduced biofilm formation.[23] Moreover, LK demonstrated anti-inflammatory capacity by reducing the secretion of IL-6.[23] Fu *et al.* proved that LK increased the viability and total alkaline phosphatase activity of osteoblasts, the number of total calcified nodules, and the expression of osteopontin and osteocalcin.[24]

Gelatin methacryloyl (GelMA) hydrogel is a frequently used hydrogel for three-dimensional cell culture and tissue engineering scaffolds,[25] polymerized under ultraviolet (UV) light in conjunction with a photo-initiator. GelMA hydrogels exhibit stability and limited antigenicity under physiological conditions. They provide a hydrated environment that facilitates cell adhesion and proliferation, rendering them highly suitable for bone tissue engineering applications.[26,27]

In this study, we developed an injectable LK-loaded GelMA hydrogel (GelMA + LK) for critical-sized bone defect regeneration (Scheme 1). We hypothesized that sustained LK release would synergistically modulate inflammation and enhance osteogenesis and angiogenesis. After material characterization and biocompatibility assessment, we evaluated (1) osteogenic potential using mouse bone marrow mesenchymal stem cells (mBMSCs); (2) angiogenic capacity through human umbilical vein endothelial cell (HUVEC) migration and tube formation; and (3) anti-inflammatory effects *via* promoting mouse monocyte macrophage leukemia cell (RAW264.7 cell) M2 macrophage polarization and scavenging ROS. Ultimately, cranial critical-sized defect models in C57/BL6 mice validated the hydrogel's *in vivo* regenerative efficacy and biocompatibility.

2. Results and discussion

2.1 Characterization and biocompatibility of LK-loaded GelMA hydrogels *in vitro*

We incorporated LK into a biocompatible GelMA hydrogel under photopolymerization to enable controlled release of LK, as shown in Fig. 1A. SEM analysis showed that both GelMA and LK-loaded GelMA hydrogels had similar interconnected microporous structures, facilitating cell attachment and substance exchange with the external environment (Fig. 1B and C). The swelling rate is important to the mechanical force of the bioactive scaffold.[28] Obtained results illustrated that the swelling rate of LK-loaded GelMA hydrogels was comparable to that of GelMA hydrogels (Fig. 1D). As for degradation, both GelMA and LK-loaded GelMA hydrogels were almost completely degraded in PBS buffers (pH 7.2–7.4) on day 12 (Fig. 1E). LK-loaded GelMA hydrogels released LK in a constant and sustained manner in 6 days (Fig. 1F). Fig. 1G showed that the LK-loaded GelMA hydrogel could be easily transferred into a syringe and extruded from a needle (0.5 × 20 mm) to form an "I" shape without any clogging. To assess the viscoelastic

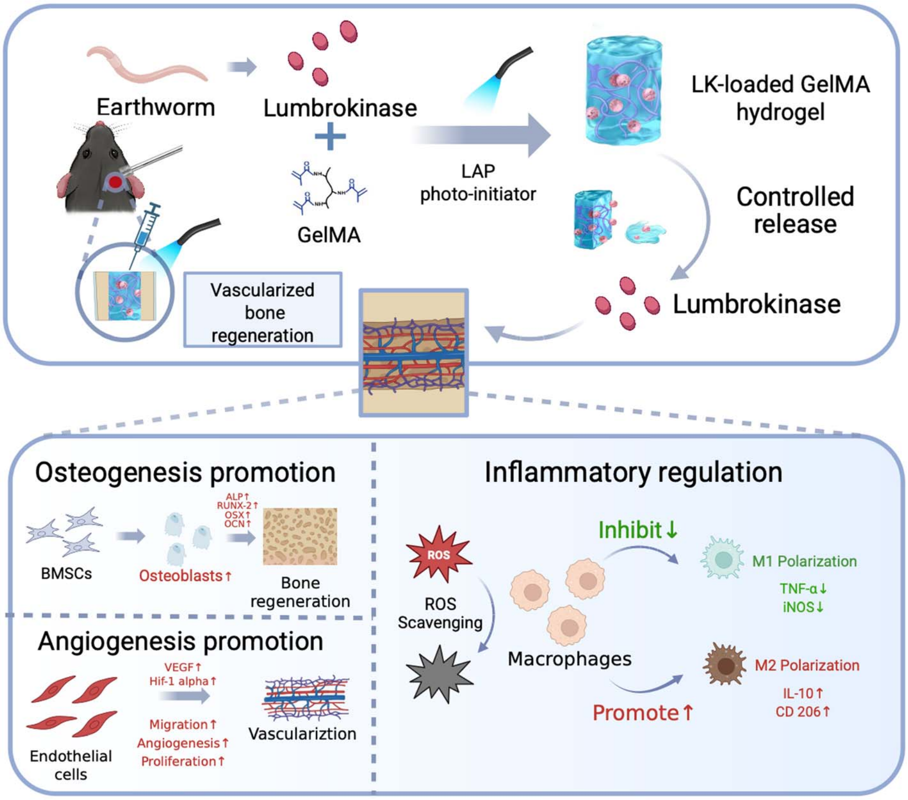

Scheme 1 Schematic diagram illustrating the constitution of the LK-loaded GelMA hydrogel and its LK sustained-release for bone defect repair by enhancing angiogenesis, osteogenesis, and inflammatory regulation.

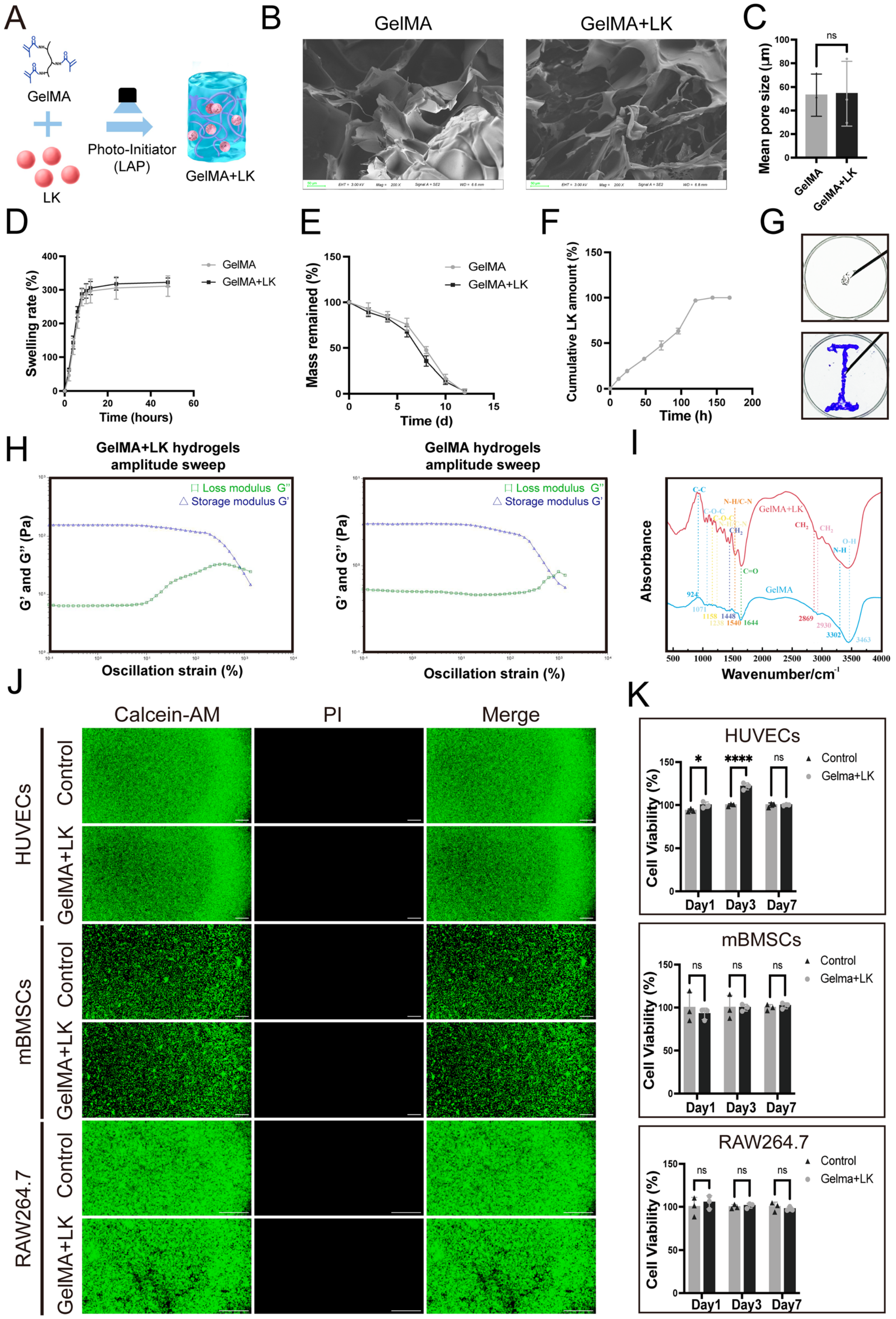

Fig. 1 Characterization and *in vitro* biocompatibility of hydrogels. (A) Schematic diagram illustrating the preparation process of LK-loaded GelMA (GelMA + LK) hydrogels. (B) Cross-section image of hydrogels (SEM), scale bars, 50 μm. (C–E) Mean pore size, swelling rate, and degradation of hydrogels, $n = 3$. (F) Cumulative release profile of LK from GelMA + LK hydrogels, $n = 3$. (G) Injectability of LK-loaded GelMA (GelMA + LK) hydrogels. (H) Amplitude sweeps showing storage modulus (G') and loss modulus (G'') of GelMA and GelMA + LK hydrogels performed over the whole strain range at a frequency of 1 Hz. (I) Fourier-transform infrared (FTIR) spectra of GelMA and GelMA + LK hydrogels. (J) Representative image of calcein AM/PI staining of HUVECs, mBMSCs, and RAW264.7 cells. Green colors represent live cells, and red colors represent dead cells. Scale bars, 100 μm. (K) Cell viability rate of HUVECs, mBMSCs, and RAW 264.7 cells, detected by CCK-8 assay, $n = 3$, $*p < 0.05$, $****p < 0.0001$.

properties of LK-loaded GelMA hydrogels, amplitude sweep test was conducted (Fig. 1H). Results showed that LK-loaded GelMA hydrogels and GelMA hydrogels had similar viscoelastic properties with $G'/G'' \gg 1$, showing a strong hydrogel character. Subsequently, we explored more detailed chemical characterization of LK-loaded GelMA hydrogels using Fourier-transform infrared (FTIR) analysis (Fig. 1I). FTIR spectra of GelMA hydrogels showed specific vibrations around 3463 cm^{-1} and 3302 cm^{-1}, corresponding to the O–H and N–H stretching, characterizing the amino and hydroxyl groups of gelatin.[29] The peaks at 2930 cm^{-1} and 2869 cm^{-1}, indicative of the antisymmetric and symmetric stretching vibrations of the CH_2 groups, demonstrated the presence of aliphatic side chains in the gelatin backbone.[30] Finally, the peak at 1644 cm^{-1} corresponded to the C═O bond (amide I vibration). To sum up, the aforementioned results confirmed the material characterization of GelMA hydrogels, aligning with previous findings.

In addition to the inherent vibrations of GelMA hydrogels, LK-loaded GelMA hydrogels presented peaks at around 1540 cm^{-1}, corresponding to the coupling of the N–H bending vibration and the C–N stretching vibration (amide II vibration). The peaks at around 1448 cm^{-1} and 1238 cm^{-1} were attributed to the bending vibration of CH_2 and the coupling of the C–N stretching vibration and N–H bending vibration (amide III vibration). Besides, the peaks at 1158 cm^{-1} and 1071 cm^{-1} were related to the C–O–C stretching in the carbohydrate or ester components of LK,[31] and the peak at 924 cm^{-1} corresponded to the backbone of C–C vibration. Finally, the peak at 1644 cm^{-1} significantly augmented, whereas the amide I band remained not displaced, proving that LK did not disrupt the protein backbone of GelMA hydrogels and was effectively solubilized into them.

In conclusion, LK-loaded GelMA hydrogels released LK in a sustained manner and exhibited comparable material characterization to GelMA hydrogels.

The *in vitro* biocompatibility of LK-loaded GelMA hydrogels was evaluated by live/dead staining and cell counting kit-8 (CCK-8) assay. After 7 days of culturing, RAW264.7 cells, mBMSCs, and HUVECs were subjected to calcein AM and propidium iodide (calcein AM/PI) staining. The results verified that the majority of cells were viable. No significant differences were observed between the control and LK-loaded GelMA group (Fig. 1J). CCK-8 assay of RAW264.7 cells and mBMSCs yielded similar results, demonstrating no significant differences between the control and LK-loaded GelMA group (Fig. 1K). Notably, the cell viability of HUVECs significantly increased in the LK-loaded GelMA group after 1 and 3 days of culturing, suggesting that LK-loaded GelMA hydrogels facilitated HUVEC proliferation. Collectively, the results proved that LK-loaded GelMA hydrogels possessed a favorable living condition for cells.

2.2 Osteogenesis promotion of LK and LK-loaded GelMA hydrogels *in vitro*

A schematic diagram illustrating the timeline of *in vitro* osteogenesis promotion experiments is shown in Fig. 2A. mBMSCs were isolated from the femur and tibia of C57/BL6 mice and identified by flow cytometry as described in Experimental Section 4.6. The expression of mBMSC markers, including positive markers (CD29 and CD44) and negative markers (CD3, CD45, and CD11b),[32] was assessed by flow cytometry. The results revealed that the positive rates of CD29, CD44, CD3, CD45, and CD11b on the isolated mBMSCs were 99.8%, 96.6%, 2.54%, 4.61%, and 5.87%, respectively (Fig. 2B). Based on the obtained results, we concluded that the isolated cells were mBMSCs.

Alkaline phosphatase (ALP), a membrane-bound glycoprotein synthesized by active osteoblasts, serves as a significant marker of osteoblast differentiation and early stages of bone mineralization. Calcium deposition is also an important feature of osteoblast differentiation and maturation. To assess osteoblast differentiation of mBMSCs, we performed ALP staining, ALP activity analysis, alizarin red S (ARS) staining, and ARS quantitative analysis.

As presented in Fig. 2C, the LK group exhibited stronger ALP staining intensity compared with the control group. The quantitative analysis of ALP activity also indicated that the LK group displayed significantly higher ALP activity compared with the control group. Similar results were observed for calcium deposition using ARS staining and quantitative analysis; the quantity of positively stained areas and mineralized nodules of calcium deposition was significantly augmented in the LK group (Fig. 2D). To investigate the effect of LK on osteogenic differentiation of mBMSCs at the molecular level, we evaluated the expression of osteogenic differentiation-related markers, including osteocalcin (OCN), osterix (OSX), runt-associated transcription factor (Runx-2), and ALP by qPCR. As shown in Fig. 2E, compared with the control group, the expressions of all the aforementioned genes were significantly upregulated in the LK group after 3 days of treatment.

We inoculated mBMSCs on GelMA and LK-loaded GelMA hydrogels in order to validate the effect of LK-loaded GelMA hydrogels on osteogenesis promotion. Similarly, the LK-loaded GelMA group showed marked elevation in ALP staining, ALP activity analysis, ARS staining, and ARS quantitative analysis (Fig. 2F and G). At the molecular level, the expressions of OCN, OSX, ALP, and Runx-2 were also significantly upregulated in the LK-loaded GelMA group after 3 days of treatment (Fig. 2H). To further evaluate the osteogenesis-promoting capacity of LK-loaded GelMA hydrogels, we cultured mBMSCs within the hydrogels and performed ALP staining. The results (SI 1A) proved that LK-loaded GelMA hydrogels also promoted osteogenesis when mBMSCs were cultured within the hydrogels. In summary, the aforementioned results proved that LK and LK-loaded GelMA hydrogels possessed the potential to enhance the osteogenic differentiation of mBMSCs *in vitro*.

2.3 Angiogenesis Promotion of LK-loaded GelMA hydrogels *in vitro*

Peripheral blood supplies in bone defects influence new bone formation because bone regeneration occurs simultaneously with blood vessel formation.[33] The migration of endothelial

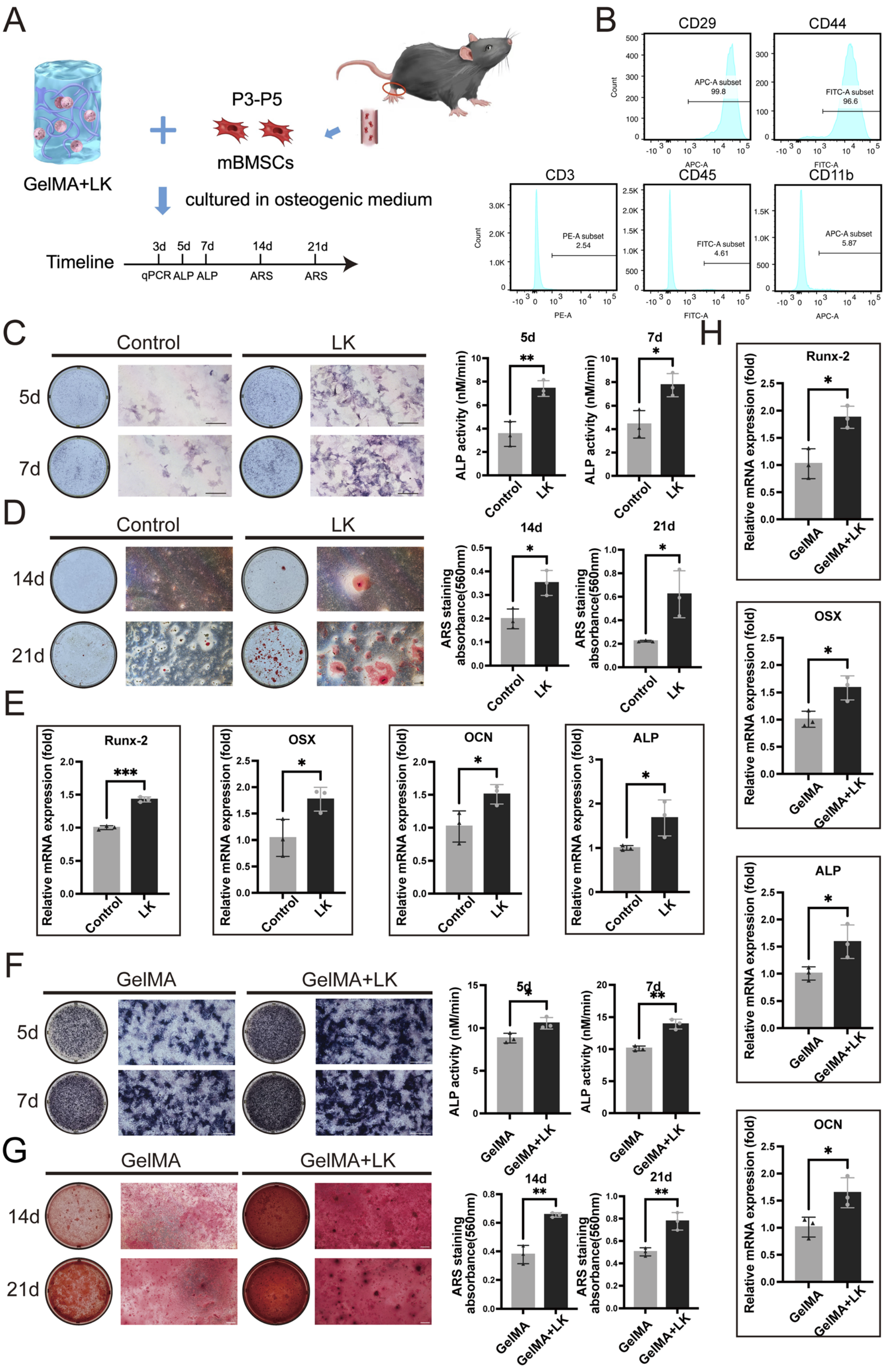

Fig. 2 Osteogenesis promotion of LK and LK-loaded GelMA (GelMA + LK) hydrogel *in vitro* (A) schematic diagram illustrating the timeline of *in vitro* osteogenesis promotion experiments. (B) The expression of positive markers (CD29 and CD44) and negative markers (CD3, CD45, and CD11b) was examined by flow cytometry for the identification of isolated mBMSCs. (C) Representative image of ALP staining and ALP activity in the control and LK group, with blue and purple colors representing positive cells, scale bar, 100 μm, $n = 3$, $*p < 0.05$, $**p < 0.01$. (D) Representative image and quantitative analysis of ARS staining in the control and LK group, with red color representing calcium deposits, scale bar, 100 μm, $n = 3$, $*p < 0.05$. (E) Relative mRNA expression levels of OCN, OSX, ALP, and Runx-2 in the control and LK group, $n = 3$, $*p < 0.05$, $***p < 0.001$. (F) Representative image of ALP staining and ALP activity in the GelMA and LK-loaded GelMA group, scale bar, 100 μm, $n = 3$, $*p < 0.05$, $**p < 0.01$. (G) Representative image and quantitative analysis of ARS staining the GelMA and GelMA + LK group, scale bar, 100 μm, $n = 3$, $**p < 0.01$. (H) Relative mRNA expression levels of OCN, OSX, ALP, and Runx-2 in the GelMA and GelMA + LK group, $n = 3$, $*p < 0.05$.

cells happens at the initial stage of angiogenesis.[34] Transwell and scratched wound assays showed that the number of migrated cells and the area of cell migration significantly increased in the LK and LK-loaded GelMA group, implying that LK-loaded GelMA hydrogels promoted the migration of endothelial cells (Fig. 3A–D). Subsequently, the effect of LK-loaded GelMA on angiogenesis was simulated *in vitro* by inoculating HUVECs on GelMA and LK-loaded GelMA hydrogels. The results showed that the total length and the number of nodes and junctions increased in the LK-loaded GelMA group (Fig. 3E).

We evaluated the expression of angiogenesis-related markers by qPCR, including vascular endothelial growth factor-*A* (VEGF)

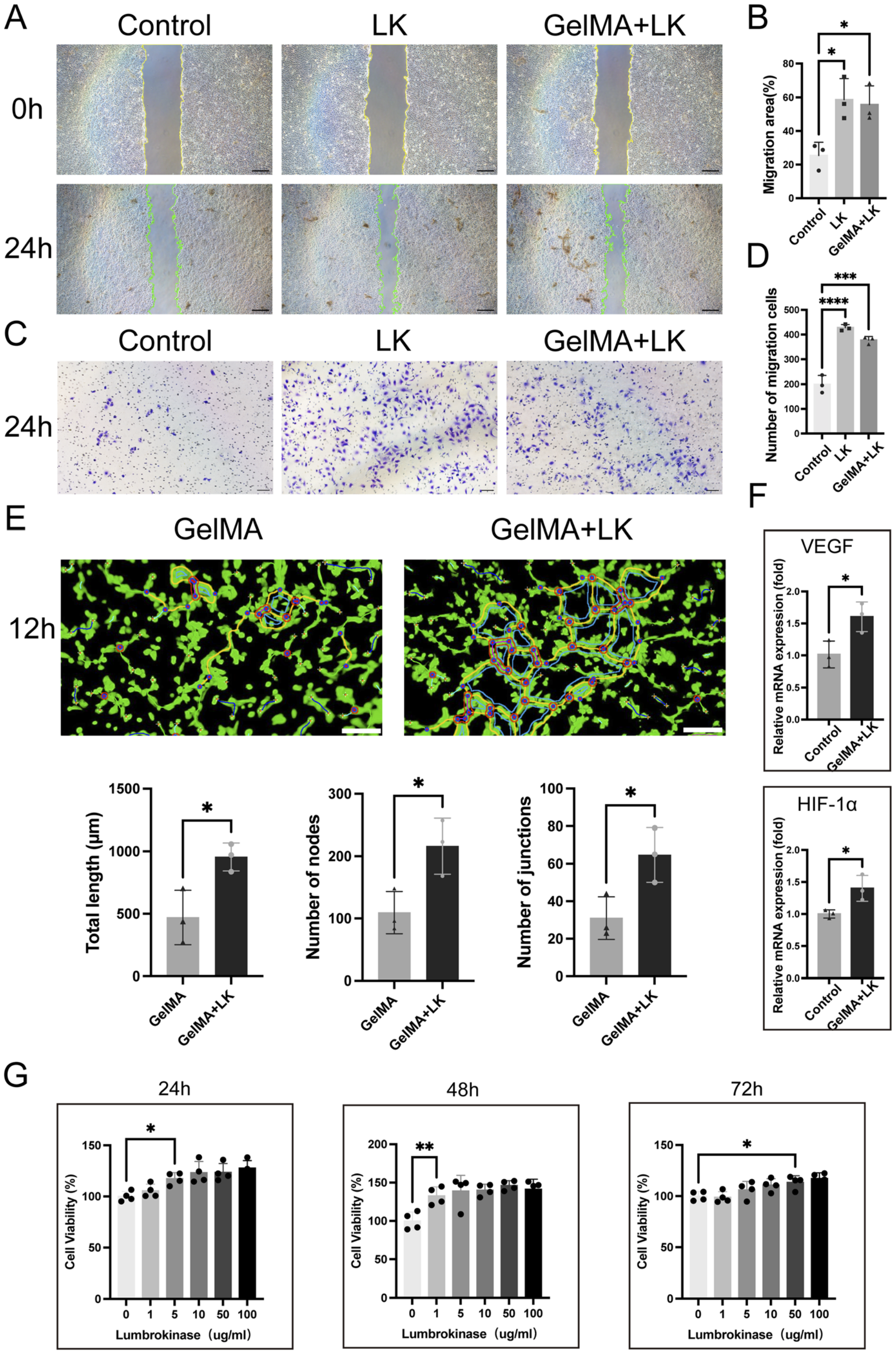

Fig. 3 Angiogenesis Promotion of LK-loaded GelMA (GelMA + LK) hydrogels *in vitro* (A) and (B) scratched wound assays and quantitative analysis of different groups, scale bar, 100 μm, $n = 3$, $*p < 0.05$. (C) and (D) Transwell tests and quantitative analysis of different groups, with purple color representing migrated cells, scale bar, 100 μm, $n = 3$, $***p < 0.001$, $****p < 0.0001$. (E) Representative images and quantitative analysis of angiogenesis tests. The yellow lines represented the formed closed loop, and the red dots represented the formed nodes, demonstrating angiogenesis capacity, scale bar, 100 μm, $n = 3$, $*p < 0.05$. (F) Relative mRNA expression levels of HIF-1α and VEGF after different treatments for 3 d, $n = 3$, $*p < 0.05$. (G) Cell viability rate of HUVECs, detected by CCK-8 assay, $n = 3$, $*p < 0.05$, $**p < 0.01$.

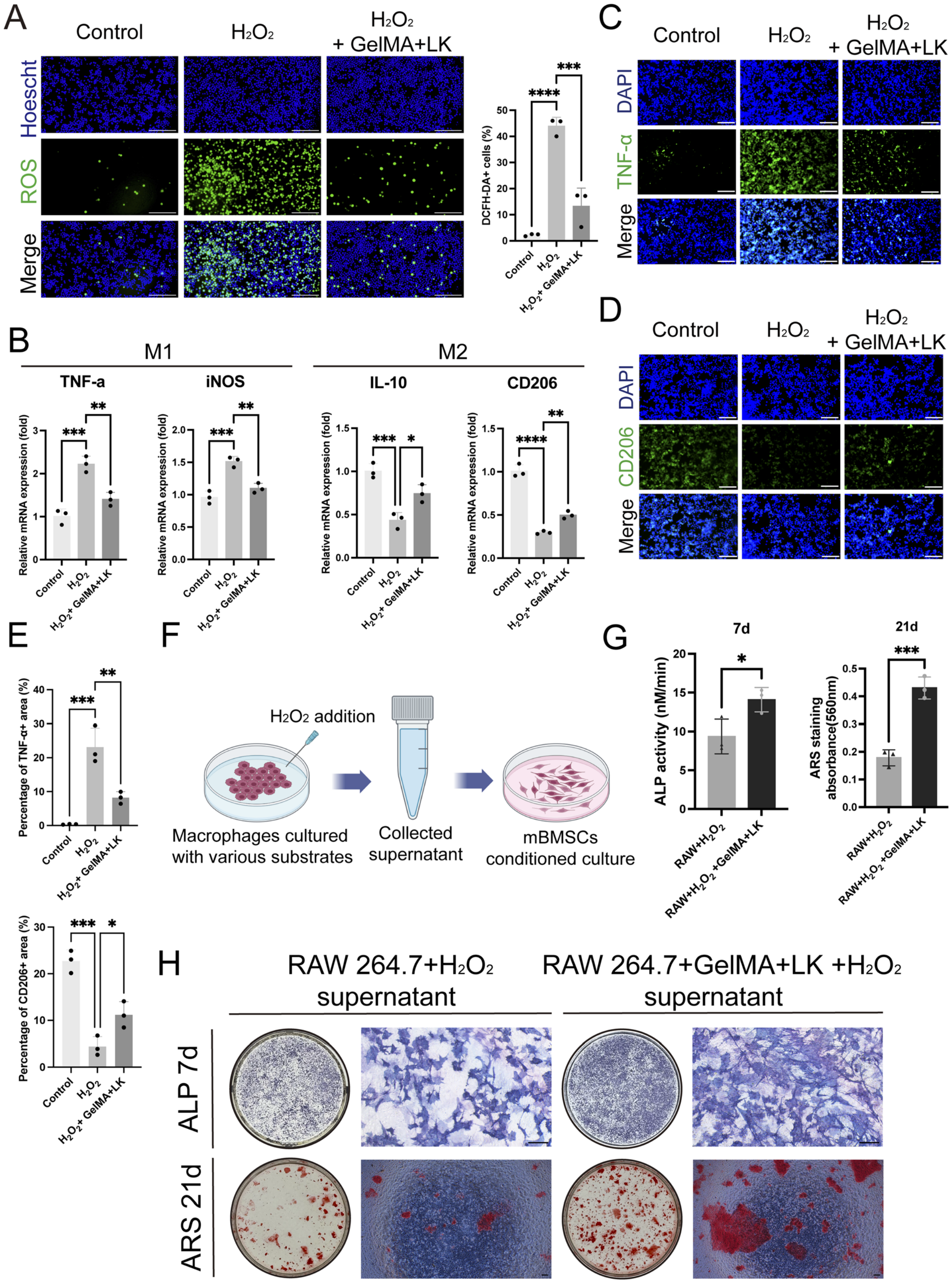

Fig. 4 Inflammatory regulation of LK-loaded GelMA (GelMA + LK) hydrogel *in vitro* (A) Representative images and quantitative analysis of DCFH-DA staining of ROS for RAW264.7 cells in different groups, scale bar, 100 μm, $n = 3$, $***p < 0.001$, $****p < 0.0001$. (B) Relative mRNA expression levels of iNOS and TNF-α (M1 hallmark indicators), IL-10 and CD206 (M2 hallmark indicators) in different groups, $n = 3$, $*p < 0.05$, $**p < 0.01$, $***p < 0.001$, $****p < 0.0001$. (C–E) Representative images and quantitative analysis of immunofluorescence staining of TNF-α (an M1 hallmark indicator) and CD206 (an M2 hallmark indicator) in RAW264.7 cells, scale bar, 100 μm, $n = 3$, $*p < 0.05$, $**p < 0.01$, $***p < 0.001$. (F) Schematic diagram illustrating the process of conditioned-culturing mBMSCs. The collected cell supernatants in the RAW264.7 cell polarization experiments were mixed with fresh Dulbecco's modified eagle's medium/F12 (DMEM/F12) at a ratio of 1 : 1 to further culture mBMSCs. (G) and (H) Representative images and quantitative analysis of ALP staining, activity, and ARS staining, scale bar, 50 μm, $n = 3$, $*p < 0.05$, $***p < 0.001$.

and hypoxia-inducible factor-1 alpha (HIF-1α). HUVECs were inoculated on LK-loaded GelMA hydrogels for 3 d before RNA extraction and qPCR. VEGF serves as a crucial regulator of angiogenesis and can indirectly connect angiogenesis to osteogenesis through its effects on endothelial cells, while also directly regulating osteoblasts.[35] HIF-1α is also a critical regulator in enhancing tissue regeneration and angiogenesis.[36] As shown in Fig. 3F, the expression of VEGF and HIF-1α significantly increased in the LK-loaded GelMA group. CCK-8 assays were conducted (Fig. 3G) to evaluate the effect of LK on the proliferative capacity of HUVECs *in vitro*. Results found that at concentrations from 5 $\mu g\ mL^{-1}$ to 100 $\mu g\ mL^{-1}$, LK significantly promoted cell proliferation after culture for 24 h. At doses ranging from 1 $\mu g\ mL^{-1}$ to 100 $\mu g\ mL^{-1}$ after culture for 48 h, LK significantly promoted cell proliferation. Finally, following a 72-hour culture, LK promoted cell proliferation at concentrations from 50 $\mu g\ mL^{-1}$ to 100 $\mu g\ mL^{-1}$. Furthermore, the aforementioned results of CCK-8 assays of HUVECs cultured on LK-loaded GelMA hydrogels, illustrated in Fig. 1H, indicated that LK-loaded GelMA hydrogels also enhanced HUVEC proliferation. In conclusion, the aforementioned results proved that LK-loaded GelMA hydrogels possessed the capacity to promote angiogenesis, migration, and proliferation of endothelial cells *in vitro*.

2.4 Inflammatory regulation of LK-loaded GelMA hydrogel *in vitro*

Bone comprises various tissues, and their interplay is essential for maintaining the balance of bone turnover. The role of macrophages in the process of bone turnover is crucial.[34] Macrophages undergo polarization, responding to diverse stimuli. The M1 type is pro-inflammatory and detrimental to osteogenic differentiation, while the M2 type, recognized as anti-inflammatory, has been shown to regulate the differentiation of BMSCs.[37,38] In the challenging microenvironment of critical-sized bone defects, continuous macrophage activation often results in the overproduction of ROS.[13] Excessive ROS can cause cellular damage and induce oxidative stress through multiple pathways, thus hindering bone regeneration in critical-sized bone defects.[12,39] Consequently, we explored the potential of LK-loaded GelMA hydrogels to create an ideal environment for bone regeneration by modulating ROS production and macrophage polarization to enhance osteogenic differentiation.

To investigate the capacity of LK-loaded GelMA hydrogels on attenuating ROS production, intracellular ROS levels in RAW264.7 cells were quantified by the fluorescent probe 2′,7′-dichlorofluorescein diacetate (DCFH-DA). Results demonstrated that the intracellular ROS level in the LK-loaded GelMA group markedly decreased upon the stimulation of hydrogen peroxide (H_2O_2), indicating its potent ROS-scavenging capability (Fig. 4A). Next, we evaluated the effect of LK-loaded GelMA hydrogels on the polarization of RAW264.7 cells by qPCR (Fig. 4B). The relative expression of M1 hallmark indicators (iNOS and TNF-α) increased significantly, while the expression of M2 hallmark indicators (IL-10 and CD206) decreased upon H_2O_2 stimulation. After adding LK-loaded GelMA hydrogel extracts, the results showed that LK-loaded GelMA hydrogels upregulated M2 marker expression and suppressed the elevation of M1 marker expression. To further verify the impact of LK-loaded hydrogels on M2 macrophage polarization, immunofluorescence staining of RAW 264.7 cells was conducted. Similarly, as shown in Fig. 4C–E, LK-loaded GelMA hydrogels inhibited the expression of TNF-α (M1 marker) and promoted CD206 (M2 marker) expression compared with the H_2O_2-treated group.

Furthermore, to verify that LK-loaded GelMA hydrogels can promote the osteogenic differentiation of mBMSCs *via* modulating M2 macrophage polarization and ROS scavenging, the cell supernatants in the aforementioned macrophage polarization experiments were collected for subsequent culture of mBMSCs (Fig. 4F). The results proved that the RAW264.7 + H_2O_2+ LK-loaded GelMA supernatant group exhibited stronger ALP staining intensity and increased ALP activity compared with the RAW264.7 + H_2O_2 supernatant group (Fig. 4G and H). Similar results were observed for calcium deposition using ARS staining and quantitative analysis (Fig. 4G and H). To sum up, LK-loaded GelMA hydrogels can promote the osteogenic differentiation of mBMSCs *via* modulating M2 macrophage polarization and scavenging ROS.

2.5 Biocompatibility and vascularized bone regeneration promotion of LK-loaded GelMA hydrogels *in vivo*

The efficacy of LK-loaded GelMA hydrogels for *in vivo* bone regeneration was evaluated using a mouse model of critical-sized cranial bone defect (Fig. 5A). Micro-CT showed that the LK-loaded GelMA group exhibited the best healing compared with the control and GelMA group (Fig. 5B and C). The bone volume/total volume (BV/TV), relative bone growth surface area, and trabecular number (Tb. N) in the LK-loaded GelMA group exceeded that of the control group and GelMA group. Trabecular separation (Tb. Sp) significantly decreased in the LK-loaded GelMA group, which was consistent with the aforementioned results.

To further investigate the effect of LK-loaded GelMA hydrogels on bone repair, histological evaluation was conducted using hematoxylin and eosin (H&E) staining, Masson's trichrome staining, and tartrate-resistant acid phosphatase (TRAP) staining (Fig. 5D). H&E staining demonstrated that the LK-loaded GelMA exhibited the highest amount of bone tissue compared to the GelMA and control group. New bone tissues were mainly distributed at the periphery of the defect region. Masson's trichrome staining confirmed the greatest quantity of new bone formation in the LK-loaded GelMA group. Osteoclasts can be visualized by TRAP staining, presenting as large cells with red cytoplasm. Results revealed that few TRAP-positive (TRAP+) osteoclasts were present at the edge of the defects in the control group and LK-loaded GelMA group, while no TRAP+ osteoclasts were found at the center of the defect in the control group and LK-loaded GelMA group. However, more TRAP+ osteoclasts were observed at both the edge and the center of the defects in the GelMA group, proving the potential of LK-loaded

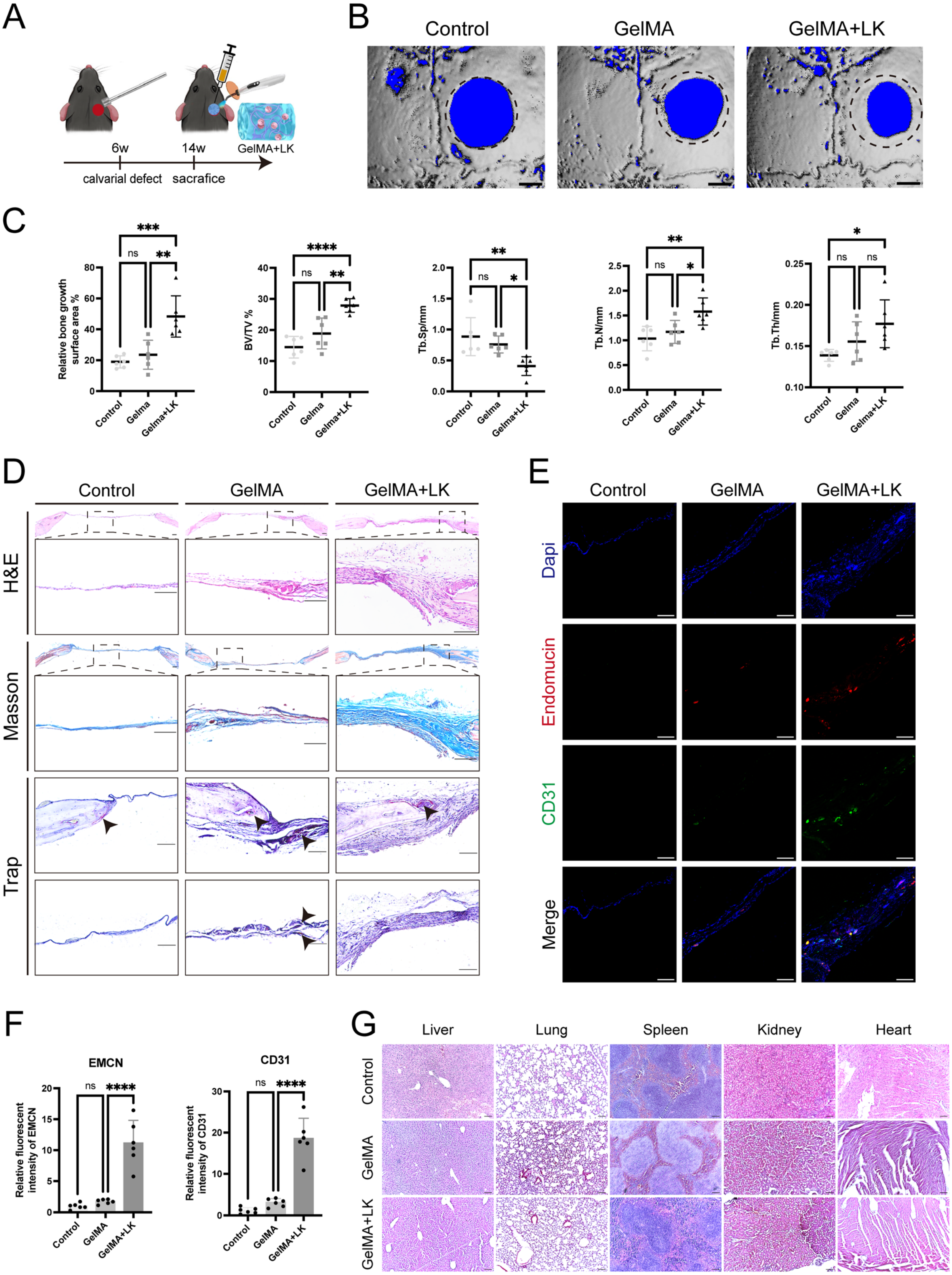

Fig. 5 Biocompatibility and vascularized bone regeneration promotion of LK-loaded GelMA (GelMA + LK) hydrogels *in vivo* (A) schematic diagram illustrating the process of establishing cranial critical-sized bone defects in mice. (B) Representative Micro-CT images of cranial critical-sized defects of different groups after 8 weeks, scale bar, 1 mm. (C) The statistical data of Micro-CT showed the parameters of bone volume/total volume (BV/TV), relative bone growth surface area, trabecular number (Tb. N), separation (Tb. Sp), and thickness (Tb. Th), $n = 6$, $^*p < 0.05$, $^{**}p < 0.01$, $^{***}p < 0.001$, $^{****}p < 0.0001$. (D) Representative images of H&E, Masson's trichrome, and TRAP staining of cranial critical-sized defects of different groups after 8 weeks, scale bar, 100 μm. (E) and (F) Representative images and quantitative analysis of immunofluorescence staining of CD31 and Endomucin of cranial critical-sized defects of different groups at 8 weeks, scale bar, 20 μm, $n = 6$, $^{****}p < 0.0001$. (G) Representative images of H&E staining of major organs in different groups, demonstrating *in vivo* biocompatibility, scale bar, 100 μm.

GelMA hydrogels to inhibit osteoclast activity. Previous studies found that LK could reduce the total TRAP activity of osteoclasts *in vitro*,[24] which was consistent with our findings.

Angiogenesis is essential for bone regeneration,[40] particularly Type H vessels, which can actively modulate bone formation by producing factors that promote the proliferation and differentiation of osteoprogenitors in the bone marrow.[33,41] Type H vessels are characterized by high expression of CD31 and endomucin 33. Consequently, we conducted tissue immunofluorescence staining to measure the expression of CD31 and endomucin. The results revealed that the expression of CD31 and endomucin was highest in the LK-loaded GelMA group compared with the control group and the GelMA group (Fig. 5E and F), demonstrating that LK-loaded GelMA hydrogels promoted vascular regeneration *in vivo*.

Major organs, including hearts, livers, spleens, lungs, and kidneys, were collected and histologically stained to verify the *in vivo* biocompatibility of LK-loaded GelMA hydrogels. H&E staining (Fig. 5G) revealed that major organs of the LK-loaded GelMA group did not exhibit significant damage or inflammation.

Collectively, these findings indicated that LK-loaded GelMA hydrogels possessed good *in vivo* biocompatibility and could promote vascularized bone regeneration in critical-sized bone defects *in vivo*.

3. Conclusion

In order to treat critical-sized bone defects, we incorporated LK into GelMA hydrogels to enable controlled release of LK. Injectable GelMA hydrogels were utilized as the scaffold. The introduction of LK did not alter the material characterization of GelMA hydrogels. LK-loaded GelMA hydrogels exhibited a porous structure, optimal swelling characteristics, tunable degradation kinetics, and good viscoelastic properties. *In vitro* experiments demonstrated that LK-loaded GelMA hydrogels can directly promote osteogenesis and angiogenesis. Furthermore, LK-loaded GelMA hydrogels upregulated the polarization of M2-type macrophages and exhibited ROS scavenging capacity, fostering a conducive immune environment for osteogenic differentiation. *In vivo*, we proved that LK-loaded GelMA hydrogels stimulated vascularized bone regeneration in a mouse critical-sized bone defect model.

The combination of LK and GelMA hydrogels not only enabled the sustained release of bioactive LK but also preserved the optimal material characteristics of GelMA hydrogels, confirming the excellent application of GelMA hydrogels as bioactive scaffolds. Additionally, we verified the osteogenic potential of LK-loaded GelMA hydrogels when used in the 3D culture of mBMSCs, further confirming the excellent biocompatibility of GelMA hydrogels when used in 3D cell culture. In this investigation, GelMA hydrogels offered an effective approach for the controlled release of traditional Chinese medicine and demonstrated its potential in 3D cell culture.

However, there are certain limitations to this study. The in-depth mechanism involved in LK's capacity of modulating M2 macrophage polarization remained to be studied. Besides, more quantitative data on cytokines needed to be included to make this study more comprehensive.

To sum up, we developed an injectable LK-loaded GelMA hydrogel with controlled release of LK for inflammatory regulation and promoting osteogenesis and angiogenesis, thereby accelerating vascularized bone regeneration.

4. Experimental section/methods

4.1 Materials

Lumbrokinase was purchased from Shanghai Maokang Biotechnology Co., Ltd. GelMA and lithium phenyl (2,4,6-trimethylbenzoyl) phosphinate (LAP) were purchased from Shenzhen Huanova Biotechnologies Co., Ltd. Mouse monocyte macrophage leukemia cells (RAW264.7) were purchased from ATCC (USA). Human umbilical vein vascular endothelial cells (HUVECs) were obtained from Shanghai Zhong Qiao Xin Zhou Biotechnology Co., Ltd. Dulbecco's modified eagle's medium/F12 (DMEM/F12), phosphate-buffered saline (1×), alpha minimum essential medium (αMEM), penicillin–streptomycin, and EDTA-free trypsin were purchased from Gibco (Shanghai, China). Dexamethasone, β-glycerophosphate sodium salt hydrate, and L-ascorbic acid were purchased from Sigma-Aldrich (USA). Fetal bovine serum (FBS) was purchased from ExCell (Shanghai, China). Calcein/PI cell viability/cytotoxicity assay kit, cell counting kit-8 (CCK-8), BCIP/NBT alkaline phosphatase (ALP) color development kit, DAPI, ALP assay, and 2′,7′-dichlorofluorescin diacetate (DCFH-DA) assay kit were purchased from Beyotime Biotechnology (Shanghai, China). The Alizarin red S (ARS) staining kit was purchased from Oricell (Guangzhou, China). Masson's Trichrome and hematoxylin & eosin (H&E) staining kits were purchased from Beijing Solarbio Science & Technology Co., Ltd. The tartrate-resistant acid phosphatase (TRAP) staining kit was purchased from Servicebio (Wuhan, China). Donkey anti-rat IgG (H + L) Alexa Fluor 594 secondary antibody (1 : 100 in immunofluorescence) was purchased from Yeasen (Shanghai, China). Donkey anti-goat IgG (H + L) Alexa Fluor 647 secondary antibody (1 : 1000 in immunofluorescence) was purchased from Invitrogen (USA). Anti-TNF-α antibody (1 : 200 in immunofluorescence) was purchased from Affinity (China). Anti-CD206 antibody (1 : 200 in immunofluorescence) was purchased from Hangzhou Huaan Biotechnology Co., Ltd. (China). Anti-endomucin antibody (1 : 200 in immunofluorescence) was purchased from Santa Cruz Biotechnology Co., Ltd. Anti-CD31 antibody (1 : 200 in immunofluorescence) was purchased from R&D Systems (USA). APC-anti-CD29, FITC-anti-CD44, PE-anti-CD3, FITC-anti-CD45, and APC-anti-CD11b antibodies were purchased from Biolegend (USA). All chemicals were used as received without further purification.

4.2 Preparation of LK-loaded GelMA hydrogels

GelMA was dissolved in αMEM in a beaker at 40 °C for 30 min. Subsequently, LAP and LK were added to the GelMA solution and continuously stirred at 40 °C for 30 min. The LK-loaded GelMA hydrogel pre-polymer was obtained successfully.

Subsequently, the pre-polymer can be cured under a temporary UV light source (405 nm) for 1 minute.

4.3 Scanning electron microscopy (SEM)

The SEM (ZEISS, Gemini SEM 300) was conducted to observe the porous structure of the hydrogel. Different hydrogels were freeze-dried using a LaboGene CoolSafe at −110 °C for 24 hours. The surfaces of lyophilized hydrogel samples were coated with gold–palladium for 45 s (Quorum SC7620). SEM images were acquired at a shooting voltage of 3 kV.

4.4 Swelling test

In order to assess the swelling capacity of LK-loaded GelMA and GelMA hydrogels, hydrogel samples were cured in a standard mold after exposure to a temporary UV light source (405 nm) for 1 m. The hydrogels were weighed to determine their initial weight (W1). Subsequently, these samples were immersed in PBS at 37 °C. The swelling weight (W_2) was measured and recorded at different time points. The swelling rate was calculated as $Q = (W_2 - W_1)/W_1 \times 100\%$.

4.5 *In vitro* degradation test and cumulative release profile

After fabricating different hydrogels as previously described (4.4 Swelling test), the samples were immersed in 10 mL of PBS at 37 °C. At specific time points (2, 4, 6, 8, 10, and 12 days), 10 mL of PBS was removed, and 10 mL of fresh PBS was added to immerse the samples. Subsequently, the samples were weighed (W_2) at different time points, and the dry weight at day 0 was recorded as (W_1). The degradation rate was calculated as $\mathrm{DR} = (W_1 - W_2)/W_1 \times 100\%$.

The standard concentration curve equation for LK was established at first. OD values at 278 nm for LK were evaluated using a photometer, and the standard concentration curves were plotted using Microsoft Excel 2019. Following the calculation, the standard concentration curve equation for LK was $y = 0.7935x + 0.0075$, $R^2 = 0.9988$. The LK release properties from the LK-loaded GelMA hydrogels were conducted in 50 mL PBS at 37 °C. 2 mL of release medium was taken out at specific time points (0, 12, 24, 48, 72, 96, 120, 144, and 168 hours), while 2 mL of fresh PBS was added in time. The cumulative LK release amount was calculated as $A = (50 \times C_n + 2 \times \sum_{1}^{n-1} C_x)/W_\mathrm{t} \times 100\%$ where C_n and C_x represent the drug concentration in the supernatant taken from time n and x, and W_t represents the total LK weight.

4.6 Amplitude sweep tests

Dynamic viscoelastic measurements were carried out using a TA DHR-2 Rheometer (USA) equipped with a plate-and-plate geometry (20 mm). The oscillation amplitude sweep test was conducted to determine the storage modulus (G') and loss modulus (G'') at a frequency of 1 Hz. During the rheological experiments, the temperature was maintained at 37 °C and the measuring system was covered with a humidity chamber to minimize water evaporation.

4.7 Fourier-transform infrared (FTIR) analysis

Fourier-transform infrared (FTIR) spectra of different freeze-dried hydrogels were recorded with a Thermo Scientific Nicolet iS20 (USA) spectrometer. Between 400 and 4000 cm^{-1} at 4 cm^{-1} resolutions, 32 scans were used for both reference and samples.

4.8 Cell culture and treatment

RAW264.7 cells were obtained from ATCC. HUVECs were obtained from Shanghai Zhong Qiao Xin Zhou Biotechnology Co., Ltd. RAW264.7 cells and HUVECs were cultured with DMEM/F12 supplemented with 10% FBS and 1% penicillin–streptomycin at 37 °C under 5% CO_2 conditions. Mouse bone marrow mesenchymal stem cells (mBMSCs) were isolated from the femur and tibia of C57/BL6 mice following anesthesia. After resecting both lower limbs, the bone marrow was completely flushed out of the bone cavity. mBMSCs were cultured with DMEM/F12 supplemented with 10% FBS and 1% penicillin–streptomycin at 37 °C under 5% CO_2 conditions.

Osteogenesis of mBMSCs was induced by adding 10 nM dexamethasone, 10 mM sodium β-glycerophosphate, and 50 μg per mL ascorbic acid. The control and LK groups were inoculated directly on 24-well plates. The control group was cultured with basic osteogenic medium, and the LK group was cultured with basic osteogenic medium added with LK.

In order to culture different cells on hydrogels, GelMA pre-polymers (with or without LK) were cured in 24-well plates (200 μL per well) under a temporary UV light source (405 nm) for 1 minute. Subsequently, RAW264.7 cells, mBMSCs, and HUVECs were inoculated on different hydrogels.

To inoculate mBMSCs within different hydrogels, mBMSCs were centrifuged and resuspended with different hydrogel pre-polymers (with or without LK). Subsequently, the mixtures were cured in 24-well plates (200 μL per well) under a temporary UV light source (405 nm) for 1 minute.

To investigate the effect of LK-loaded GelMA hydrogels on macrophage polarization when stimulated with H_2O_2, RAW264.7 cells were cultured in 6-well plates and treated with H_2O_2 and extracts of different hydrogels for 12 h for further RNA extraction and qPCR.

To verify that LK-loaded GelMA hydrogels can promote mBMSCs osteogenic differentiation *via* modulating M2 macrophage polarization and ROS scavenging, the macrophage conditioned medium (MCM) was collected, centrifuged at 4 °C for 1 hour, and filtered through a 0.22 μm pore filter (Millipore, USA). Then, the obtained MCM was mixed with osteogenic medium in a 1 : 2 volume ratio to induce osteogenic differentiation of mBMSCs for further experiments.

4.9 Live/dead staining

After 7 days of treatment with LK-loaded GelMA hydrogel extracts, mBMSCs, HUVECs, and RAW264.7 cells were incubated with calcein AM and propidium iodide (calcein AM/PI), following the manufacturer's instructions to stain live and dead cells. Subsequently, the cells were observed by an inverted fluorescence microscope (Zeiss, Germany).

4.10 Cell proliferation assay

The proliferation rates of mBMSCs, HUVECs, and RAW264.7 cells were assessed by CCK-8 assay. According to the manufacturer's instructions, 10% CCK-8 reagent was added on days 1, 3, and 7 of culture, and after culturing for 1 h, the absorbance of the collected supernatant at 405 nm was analyzed using a microplate reader (PerkinElmer, Finland). The cell viability was evaluated by the percent of the absorbance of cells inoculated on LK-loaded GelMA hydrogels *versus* the control group.

4.11 RNA extraction and qPCR

After different treatments, the total RNA of cells was extracted. Subsequently, the extracted RNA was reverse-transcribed to obtain complementary deoxyribonucleic acid (DNA) (cDNA). The mRNA expression of related genes was detected by qPCR. The GAPDH gene was used for normalization.

4.12 Alkaline phosphatase staining and activity assay

After 5 and 7 days of osteogenic induction of mBMSCs (as described in 4.6), alkaline phosphatase (ALP) staining was performed using the BCIP/NBT ALP Color Development Kit. According to the manufacturer's instructions, the mixture of BCIP, NBT, and working solution was added and then incubated at room temperature in the dark for 30 min. The reaction was stopped by removing the staining solution and washing with double distilled water (ddH_2O) 1–2 times. ALP of mBMSCs was extracted by adding sterilized ddH_2O after repeated freezing–thawing. The ALP activity was assessed with an ALP assay kit, following the manufacturer's instructions.

4.13 Alizarin red staining

After 14 and 21 days of osteogenic induction of mBMSCs (as described in 4.6), calcium deposition in each group was stained and analyzed using an alizarin red staining kit, following the manufacturer's instructions.

4.14 Cell migration assay

The migration capacity of HUVECs was assessed by transwell tests and scratched wound assays. Transwell chambers were placed in 24-well plates, containing basal medium (DMEM/F12) in the upper chamber and complete medium (DMEM/F12 supplemented with 10% FBS and 1% penicillin–streptomycin) in the lower chamber. The complete medium in the lower chamber was used as a chemoattractant. The cells were pre-starved for 24 h before being inoculated in the upper chamber. LK and abstracts of LK-loaded GelMA hydrogels were added separately in the LK and GelMA + LK groups.

After 24 hours of incubation, the cells in the transwell chambers were fixed with 4% paraformaldehyde and then stained with crystal violet. The cells were carefully removed with sterilized Q-tips from the upper layer and photographed using a light microscope (Leica, Germany).

In order to perform scratched wound assays, HUVECs were inoculated in 6-well plates. After they reached full confluence, they were pre-starved with basal medium for 24 h before further experiment. The cells were scratched with a 200 μL pipette to generate uniform-width wounds, rinsed with PBS, cultured with low-serum medium (DMEM/F12 supplemented with 1% FBS and 1% penicillin–streptomycin), and left to migrate for 24 h. Finally, the cell migration was photographed by a light microscope (Leica, Germany).

4.15 Tube formation assay

To simulate blood vessel formation *in vitro*, GelMA pre-polymers (with or without LK) were cured in 96-well plates (50 μL per well) under a temporary UV light source (405 nm) for 1 m. Prestarved HUVECs were inoculated on different hydrogels at a density of 30 000 per well and stained with calcein AM. Different groups were observed by an inverted fluorescence microscope (Zeiss, Germany) to assess blood vessel formation *in vitro*. The scratched wound was photographed using an inverted fluorescence microscope (Zeiss, Germany).

4.16 ROS staining

The extracts of different hydrogels were obtained by immersing samples in PBS at 37 °C for 3 days. After 24 hours of treatment with H_2O_2 and extracts of different hydrogels, RAW264.7 cells were stained with a DCFH-DA assay kit for 20 min at 37 °C. After staining with DAPI, cells were observed by an inverted fluorescence microscope (Zeiss, Germany).

4.16 Immunofluorescence staining of cells

Following various treatments, RAW264.7 cells were rinsed in PBS and fixed with 4% paraformaldehyde for 30 min, permeabilized with 0.5% Triton X-100 for 20 min, and then blocked with 10% horse serum for 90 min. The cells were incubated for 12 h at 4 °C with specific antibodies according to the manufacturer's instructions and for 60 min with fluorescent secondary antibodies protected from light. Finally, the results were visualized using fluorescence microscopy (Ti2-U, Nikon, Japan) after restaining with DAPI.

4.18 Animal model

Six-week-old male C57/BL6 mice were selected for constructing critical-sized cranial bone defects. The mice were housed in the Experimental Animal Centre of Shanghai Engineering Research Center of Tooth Restoration and Regeneration (Approval No. [2023]-DW-24), Tongji University, in an air-conditioned environment maintained at 23–25 °C with a light–dark cycle time of 12 h. The mice were randomly allocated into 3 groups with 6 in each group: a control group, a GelMA group, and an LK-loaded GelMA group. After anesthetization, the skin was prepared and incised to expose the skull. Subsequently, a 3 mm diameter defect was made using a circular bit on the skull surface. Different hydrogel pre-polymers (for the GelMA group and LK-loaded GelMA group) and αMEM (for the control group) were injected into the bone defect and cured under a temporary UV light source (405 nm) for 1 m. Finally, the wound was disinfected and sutured. All procedures and used instruments were performed in a sterile environment.

4.19 Micro-CT scanning and analysis

The mice were euthanized after 8 weeks, and the skulls were isolated and fixed in 4% paraformaldehyde for 48 h. The obtained samples were scanned with a Scanco mCT 50 (Scanco Medical, Switzerland) at a scan resolution of 10 μm and a voltage of 70 kVp. After scanning, 3D images were reconstructed. The bone volume fraction (BV/TV), trabecular separation (Tb. Sp, mm), trabecular thickness (Tb. Th, mm), and trabecular number (Tb. N, mm^{-1}) were calculated using auxiliary software.

4.20 Histological staining

After Micro-CT scanning, the specimens from different groups were decalcified in 10% ethylenediaminetetraacetic acid and embedded in paraffin. Paraffin blocks were serially cut into 4 μm sections with a microtome. The sections were deparaffinized in xylene and rehydrated with a gradient concentration of ethanol. Finally, the sections were stained using the HE, Masson's Trichrome, and TRAP staining kits and observed by light microscopy (Leica, Germany).

4.21 Immunofluorescence staining of tissues

After dewaxing and rehydrating (as described in 4.17), the sections were treated with trypsin for antigen repair and 3% H_2O_2 to eliminate endogenous peroxidase activity. Subsequently, the sections were incubated with the primary antibody at 4 °C for 12 h and the secondary antibody at room temperature for 1 h. The primary antibodies used were anti-CD31 and anti-endomucin, which were diluted in accordance with the manufacturer's instructions (as described in 4.1). Images were captured using fluorescence microscopy (Ti2-U, Nikon, Japan) after restaining with DAPI.

4.22 Flow cytometry

Following digestion and centrifugation, mBMSCs of passage 3 were resuspended and filtered using a 40 μm cell strainer. MBMSCs were stained with APC-anti-CD29, FITC-anti-CD44, PE-anti-CD3, FITC-anti-CD45, and APC-anti-CD11b antibodies for 30 minutes at 4 °C, followed by analysis using an LSRFortessa flow cytometer (BD Biosciences). Cell gating was conducted by comparing with isotype controls.

4.23 Statistical analysis

All the data were presented as the mean ± standard deviation (SD). The Student's *t*-test was employed for comparisons between two independent groups, while one-way analysis of variance (ANOVA) was used for comparisons between multiple groups. Statistical significance was established at $p < 0.05$.

Ethics statement

All animal procedures were performed in accordance with the Guidelines for Care and Use of Laboratory Animals of Shanghai Tongji Stomatological Hospital and Dental School, Tongji University (approval number: [2023]-DW-24).

Conflicts of interest

The authors declare no conflict of interest.

Data availability

The authors confirm that the data supporting the findings of this study are available within the article.

Osteogenic-promoting ability of LK-loaded GelMA hydrogels in 3D culture. See DOI: **https://doi.org/10.1039/d5ra04178c**.

Acknowledgements

This work was supported by National Natural Science Foundation of China (No. NSFC 81700978); Natural Science Foundation of Shanghai (No. 22S11902800, 22ZR1467300); Shanghai Municipal Health Commission's Clinical Research Project (202340064); and the Fundamental Research Funds for the Central Universities (22120240308). We acknowledge Jia-Ying Xin for her help with schematic illustration.

References

1 D. Tang, *et al.*, Biofabrication of bone tissue: approaches, challenges and translation for bone regeneration, *Biomaterials*, 2016, **83**, 363–382.
2 T. Gong, *et al.*, Nanomaterials and bone regeneration, *Bone Res.*, 2015, **3**, 15029.
3 V. S. Kumawat, S. Bandyopadhyay-Ghosh and S. B. Ghosh, An overview of translational research in bone graft biomaterials, *J. Biomater. Sci., Polym. Ed.*, 2023, **34**(4), 497–540.
4 X. Bai, *et al.*, Bioactive hydrogels for bone regeneration, *Bioact. Mater.*, 2018, **3**(4), 401–417.
5 R. Eastell, *et al.*, Postmenopausal osteoporosis, *Nat. Rev. Dis. Primers*, 2016, **2**, 16069.
6 G. Zhu, *et al.*, Bone physiological microenvironment and healing mechanism: Basis for future bone-tissue engineering scaffolds, *Bioact. Mater.*, 2021, **6**(11), 4110–4140.
7 E. Alarcin, *et al.*, 3D bioprinted biomimetic bilayer GelMA scaffolds for the delivery of BMP-2 and VEGF exogenous growth factors to promote vascularized bone regeneration in a calvarial defect model in vivo, *Int. J. Biol. Macromol.*, 2025, 141440.
8 T. Itkin, *et al.*, Distinct bone marrow blood vessels differentially regulate haematopoiesis, *Nature*, 2016, **532**(7599), 323–328.
9 H. Liu, *et al.*, Delivering Proangiogenic Factors from 3D-Printed Polycaprolactone Scaffolds for Vascularized Bone Regeneration, *Adv. Healthcare Mater.*, 2020, **9**(23), e2000727.

10 M. Zhang, *et al.*, 3D printing of Haversian bone-mimicking scaffolds for multicellular delivery in bone regeneration, *Sci. Adv.*, 2020, **6**(12), eaaz6725.

11 M. Wu, *et al.*, Photoactivated Hydrogel Therapeutic System with MXene-Based Nanoarchitectonics Potentiates Endogenous Bone Repair Through Reshaping the Osteo-Vascularization Network, *Small*, 2024, **20**(51), e2403003.

12 A. J. Sheppard, *et al.*, Understanding Reactive Oxygen Species in Bone Regeneration: A Glance at Potential Therapeutics and Bioengineering Applications, *Front. Bioeng. Biotechnol.*, 2022, **10**, 836764.

13 P. Qiu, *et al.*, Periosteal matrix-derived hydrogel promotes bone repair through an early immune regulation coupled with enhanced angio- and osteogenesis, *Biomaterials*, 2020, **227**, 119552.

14 Q. Huang, *et al.*, ROS-responsive hydrogel for bone regeneration: Controlled dimethyl fumarate release to reduce inflammation and enhance osteogenesis, *Acta Biomater.*, 2025, **195**, 183–200.

15 A. Lao, *et al.*, Functionalized Metal-Organic Framework-Modified Hydrogel That Breaks the Vicious Cycle of Inflammation and ROS for Repairing of Diabetic Bone Defects, *Small*, 2023, **19**(36), e2206919.

16 S. C. Johnson Retnaraj Samuel, *et al.*, Autofluorescence in BrdU-positive cells and augmentation of regeneration kinetics by riboflavin, *Stem Cells Dev.*, 2012, **21**(11), 2071–2083.

17 S. Song, *et al.*, Effect of earthworm active protein on fibroblast proliferation and its mechanism, *Pharm. Biol.*, 2016, **54**(4), 732–739.

18 H. Mihara, *et al.*, A Novel Fibrinolytic Enzyme Extracted from the Earthworm, *Lumbricus rubellus*, *Jpn. J. Physiol.*, 1991, **41**(3), 461–472.

19 I. H. Cho, *et al.*, Purification and characterization of six fibrinolytic serine-proteases from earthworm Lumbricus rubellus, *J. Biochem. Mol. Biol.*, 2004, **37**(2), 199–205.

20 L. Jin, *et al.*, Changes in coagulation and tissue plasminogen activator after the treatment of cerebral infarction with lumbrokinase, *Clin. Hemorheol. Microcirc.*, 2000, **23**(2–4), 213–218.

21 M. Kasim, *et al.*, Improved myocardial perfusion in stable angina pectoris by oral lumbrokinase: a pilot study, *J. Altern. Complementary Med.*, 2009, **15**(5), 539–544.

22 Y.-H. Wang, *et al.*, Lumbrokinase attenuates myocardial ischemia-reperfusion injury by inhibiting TLR4 signaling, *J. Mol. Cell. Cardiol.*, 2016, **99**, 113–122.

23 W. L. Wang, *et al.*, Ex Vivo Model to Evaluate the Antibacterial and Anti-Inflammatory Effects of Gelatin-Tricalcium Phosphate Composite Incorporated with Emodin and Lumbrokinase for Bone Regeneration, *Bioengineering*, 2023, **10**(8), 906.

24 Y. T. Fu, *et al.*, Porous gelatin/tricalcium phosphate/genipin composites containing lumbrokinase for bone repair, *Bone*, 2015, **78**, 15–22.

25 A. G. Kurian, *et al.*, Multifunctional GelMA platforms with nanomaterials for advanced tissue therapeutics, *Bioact. Mater.*, 2022, **8**, 267–295.

26 M. Su, *et al.*, Current state of knowledge on intelligent-response biological and other macromolecular hydrogels in biomedical engineering: A review, *Int. J. Biol. Macromol.*, 2023, **227**, 472–492.

27 L. Huang, *et al.*, Advancements in GelMA bioactive hydrogels: Strategies for infection control and bone tissue regeneration, *Theranostics*, 2025, **15**(2), 460–493.

28 M. G. Fernandes, *et al.*, Mechanomodulatory biomaterials prospects in scar prevention and treatment, *Acta Biomater.*, 2022, **150**, 22–33.

29 M. Bansal, *et al.*, An interpenetrating and patternable conducting polymer hydrogel for electrically stimulated release of glutamate, *Acta Biomater.*, 2022, **137**, 124–135.

30 Y. Ji, *et al.*, Surface Modification of WE43 Magnesium Alloys with Dopamine Hydrochloride Modified GelMA Coatings, *Coatings*, 2022, **12**(8), 1074.

31 S. K. Metkar, *et al.*, Lumbrokinase for degradation and reduction of amyloid fibrils associated with amyloidosis, *J. Appl. Biomed.*, 2017, **15**(2), 96–104.

32 B. Sun, *et al.*, Autophagy Regulates Age-Related Jawbone Loss via LepR(+) Stromal Cells, *J. Dent. Res.*, 2024, **103**(10), 1028–1038.

33 A. P. Kusumbe, S. K. Ramasamy and R. H. Adams, Coupling of angiogenesis and osteogenesis by a specific vessel subtype in bone, *Nature*, 2014, **507**(7492), 323–328.

34 J. Mao, *et al.*, Multifunctional Bionic Periosteum with Ion Sustained-Release for Bone Regeneration, *Adv. Sci.*, 2024, **11**(39), e2403976.

35 M. G. Burger, *et al.*, Robust coupling of angiogenesis and osteogenesis by VEGF-decorated matrices for bone regeneration, *Acta Biomater.*, 2022, **149**, 111–125.

36 S. Saber, *et al.*, Nanoscale Systems for Local Activation of Hypoxia-Inducible Factor-1 Alpha: A New Approach in Diabetic Wound Management, *Int. J. Nanomed.*, 2024, **19**, 13735–13762.

37 J. Liu, *et al.*, M2 macrophage-derived exosomal miR-486-5p influences the differentiation potential of bone marrow mesenchymal stem cells and osteoporosis, *Aging*, 2023, **15**(18), 9499–9520.

38 A. Dubey, *et al.*, Separate roles of IL-6 and oncostatin M in mouse macrophage polarization in vitro and in vivo, *Immunol. Cell Biol.*, 2018, **96**(3), 257–272.

39 J. S. Kimball, J. P. Johnson and D. A. Carlson, Oxidative Stress and Osteoporosis, *J. Bone Jt. Surg., Am. Vol.*, 2021, **103**(15), 1451–1461.

40 J. Cui, *et al.*, Coaxially fabricated dual-drug loading electrospinning fibrous mat with programmed releasing behavior to boost vascularized bone regeneration, *Adv. Healthcare Mater.*, 2022, **11**(16), 2200571.

41 S. K. Ramasamy, *et al.*, Endothelial Notch activity promotes angiogenesis and osteogenesis in bone, *Nature*, 2014, **507**(7492), 376–380.